RSC Advances

ROYAL SOCIETY OF CHEMISTRY

PAPER

View Article Online
View Journal | View Issue

Cite this: *RSC Adv.*, 2020, **10**, 19936

Epitaxial and large area Sb_2Te_3 thin films on silicon by MOCVD†

Martino Rimoldi,[a] Raimondo Cecchini,[a] Claudia Wiemer,[a] Alessio Lamperti,[a] Emanuele Longo,[ab] Lucia Nasi,[c] Laura Lazzarini,[c] Roberto Mantovan*[a] and Massimo Longo*[a]

Received 19th March 2020
Accepted 18th May 2020

DOI: 10.1039/d0ra02567d

rsc.li/rsc-advances

Antimony telluride (Sb_2Te_3) thin films were prepared by a room temperature Metal–Organic Chemical Vapor Deposition (MOCVD) process using antimony chloride ($SbCl_3$) and bis(trimethylsilyl)telluride ($Te(SiMe_3)_2$) as precursors. Pre-growth and post-growth treatments were found to be pivotal in favoring out-of-plane and in-plane alignment of the crystallites composing the films. A comprehensive suite of characterization techniques were used to evaluate their composition, surface roughness, as well as to assess their morphology, crystallinity, and structural features, revealing that a quick post-growth annealing triggers the formation of epitaxial-quality Sb_2Te_3 films on Si(111).

Open Access Article. Published on 27 May 2020. Downloaded on 7/22/2020 1:37:40 PM.
This article is licensed under a Creative Commons Attribution-NonCommercial 3.0 Unported Licence.

Introduction

Chalcogenide structures, such as two-dimensional layered materials,[1] thin films,[2–4] and nanowires,[5–7] recently have become technologically relevant materials in the context of memory devices and spintronics.[8]

In particular, the semiconductor antimony telluride (Sb_2Te_3) has been exploited in phase change memory cells, taking advantage of its reversible amorphous-to-crystalline transition,[9,10] as a thermoelectric material,[11–13] and more recently as a topological insulator (TI),[14,15] since it has been demonstrated, despite its insulating bulk, to possess surface Dirac cones and conductive edge states.

So far, various techniques have been reported capable of Sb_2Te_3 deposition, including microwave-assisted solvothermal synthesis,[16] sputtering,[17,18] chemical vapor deposition,[19,20] atomic layer deposition,[12,21–26] molecular beam epitaxy,[27–30] and Metal–Organic Chemical Vapor Deposition (MOCVD).[31–39]

Amongst these methods, MOCVD, an industrially ready technique historically adopted for large-scale semiconductor production and suitable for large area film growth, appears to be the preferred scale-up option in an industrial environment. The quality of the films is fundamental for their use in electronic applications. Crystalline and highly oriented materials are required to exploit their physical properties and to achieve a successful device implementation, as demonstrated for instance in the variety of successful III–V semiconductors-based devices[40,41]—the ultimate target being epitaxy and single crystal growth.

Epitaxial films of Sb_2Te_3 (and other topological insulators such as Bi_2Te_3 and Bi_2Se_3) have been straightforwardly grown by molecular beam epitaxy processes,[29,30] a technique that shows its limits in the volume production. On the other hand, chemical vapor deposition techniques suffer from poor morphology control, and we specifically investigated MOCVD with this regard.

Commonly employed substrates in TIs growth, such as Si(100), Si(111), and Al_2O_3(0001), show a significant lattice mismatch with Sb_2Te_3 (and TIs in general) that therefore grows as poorly oriented polycrystalline layers in the presence of rotational domains,[23,32–34] with only a few exceptions.[42,43] Recently, to overcome this issue, way less common materials, such as BaF_2(111)[30] and, for instance, a ZnTe or GaN buffer layer on Al_2O_3(0001), have been identified to lattice match with telluride-TIs and effectively adopted as substrates to enhance the quality of the films.[30,35] Most significantly, the large area deposition of high-quality Sb_2Te_3 epitaxial layers on Si substrates with thickness control below 100 nm would be much attractive for integration in CMOS compatible devices.

Specific to MOCVD processes, alike other chemical methods, the selection of precursors plays a relevant role in governing the growth and morphology of the films.

So far, the most promising results in Sb_2Te_3 growth were achieved employing trialkylstibines (such as $SbMe_3$, Sb^iPr_3) and diallyltellanes ($TeEt_2$, Te^iPr_2) as precursors; however, temperatures greater than or equal to 400 °C were required, along with a dihydrogen partial pressure, to sustain the precursors'

[a]Institute for Microelectronics and Microsystems, CNR-IMM Unit of Agrate Brianza, Via C. Olivetti 2, 20864, Agrate Brianza, Italy. E-mail: massimo.longo@mdm.imm.cnr.it; roberto.mantovan@mdm.imm.cnr.it

[b]University of Milano-Bicocca, Department of Material Science, Via R. Cozzi 55, 20126, Milan, Italy

[c]Institute of Materials for Electronics and Magnetism, CNR-IMEM, Parma, Parco Area delle Scienze, 7/A, 43100 Parma, Italy

† Electronic supplementary information (ESI) available: Additional SEM, AFM, and TEM images and characterization data. See DOI: 10.1039/d0ra02567d

This journal is © The Royal Society of Chemistry 2020

pyrolysis.[32,35] The more engineered species Et_2Te_2 [34,44] and $(Et_2Sb)_2Te$[33] have also been adopted for high-temperature depositions. Nevertheless, the high deposition rate required to achieve a uniform and well-oriented crystalline Sb_2Te_3 MOCVD resulted in films several hundreds of nanometers thick.[34,35]

Here, we report a room temperature (RT) MOCVD process to obtain epitaxial Sb_2Te_3 thin (30 nm) films on bare Si(111) substrates and show the effect of pre-growth (substrates annealing) and post-growth (film processing) treatments on the film morphology, surface roughness, crystallinity, and crystallographic orientation.

Experimental

Materials

The Si(111) substrates were purchased from Silicon Materials Inc. and cut in approximately 1–2 square centimeter pieces.

Sb_2Te_3 thin films by MOCVD

Prior to deposition, the Si(111) substrates were treated with HF (5% in deionized H_2O) for 3 min, thoroughly rinsed with deionized H_2O, and N_2-dried. Then, samples were quickly loaded into the glove box-protected MOCVD chamber. Sb_2Te_3 thin films were grown with an Aixtron AIX 200/4 MOCVD tool equipped with an IR-heated 4″ rotating graphite susceptor. Electronic grade precursors antimony chloride ($SbCl_3$) and bis(trimethylsilyl)telluride ($Te(SiMe_3)_2$) were supplied by Air Liquide Electronics. Precursors were loaded into bubblers thermalized at 20.0 (±0.1) °C and delivered to the MOCVD chamber through the vapor-saturated ultra-pure N_2 carrier gas. Depositions were carried out at 25 °C for 90 min at 15 mbar pressure, with a total flow of 5.575 l min^{-1}, and setting the precursors vapor pressures at 2.28 and 3.32×10^{-4} mbar for $SbCl_3$ and $Te(SiMe_3)_2$, respectively. Substrates annealing (prior to deposition) was performed *in situ* at 500 °C for 60 min at 20 mbar, with a total N_2 flow of 11.000 l min^{-1}. Post-growth films annealing was performed *in situ* according to the following routine: (1) heating ramp: 5.575 l min^{-1} N_2 flow, 900 mbar, from RT to 300 °C in 10 min; (2) annealing: 5.575 l min^{-1} N_2 flow, 900 mbar, 300 °C, 15 min; (3) cooling ramp: 1.500 l min^{-1} N_2 flow, 990 mbar, from 300 °C to 200 °C in 20 min, from 200 °C to 100 °C in 35 min, from 100 °C to 50 °C in 20 min.

Materials characterization

Scanning Electron Microscopy (SEM) images were acquired on a ZEISS Supra 40 field emission scanning electron microscope at an acceleration voltage of 15 kV. Samples were cut prior to measurement and cross-section images collected at a tilting angle of 25°. Atomic Force Microscopy (AFM) images were obtained on a Bruker Dimension Edge instrument in non-contact mode using a sharp silicon AFM probe (TESPA, Bruker) with a typical radius of curvature in the 8–12 nm range. A polynomial background correction was applied to the raw data. Surface roughness is reported as Root Mean Square roughness (RMS roughness, R_q) and expressed in nanometers. Transmission Electron Microscopy (TEM) analyses were performed using a JEOL 2200FS microscope working at 200 kV equipped with an Energy Dispersive X-ray Spectrometer (EDX), two high-angle annular dark-field (HAADF) detectors and an in-column energy (Omega) filter. The cross-sectional view samples were prepared using standard mechano-chemical procedures and finished by ion beam thinning. Total reflection X-ray Fluorescence (TXRF) measurements were performed using an X-ray total reflection spectrometer equipped with a Mo K_α radiation source. Elemental composition of the Sb_2Te_3 films was determined from the ratio of the antimony and tellurium L_α lines (Sb L_α = 3.604 keV; Te L_α = 3.768 keV). X-Ray Photoelectron Spectroscopy (XPS) data were collected on a PHI 5600 instrument (monochromatic Al K_α X-ray source, 1486.6 eV) equipped with a concentric hemispherical analyzer. After the deposition, samples were quickly transferred from the MOCVD tools into the XPS loading chamber (approximately 5 seconds of air exposure) and the spectra acquired at a 45° take-off angle. The spectra were referenced to the C 1s signal set at 284.8 eV. Te and Sb 3d and 4d spectra were recorded. X-Ray Reflectivity (XRR) and X-ray Diffraction (XRD) pattern were acquired with a HRXRD IS2000 equipped with a Cu K_α radiation source, a four circle goniometer, and a curved 120° position-sensitive detector (Inel CPS-120).

Results and discussion

The metal–organic chemical vapor deposition of antimony telluride thin films was developed at room temperature and under inert atmosphere (no dihydrogen required) taking advantage of the precursors' reactivity previously demonstrated in tellurides atomic layer deposition[21–23] and in other similar CVD processes.[45,46] Under the optimal growth conditions ($SbCl_3$ and $Te(SiMe_3)_2$ partial pressures of 2.23 and 3.25×10^{-4} mbar, respectively, a total flow of 5.575 l min^{-1}, a deposition pressure of 15 mbar, and a deposition time of 90 min) the process afforded on HF-treated Si(111) an approximately 30 nm thick continuous film.

The Sb_2Te_3 films, referred to as "Sb_2Te_3 – As Deposited" (**1**), even though continuous, exhibited a marked granularity and a non-uniform grains orientation (Fig. 1), features reminiscent of the recently reported Sb_2Te_3 MOCVD on SiO_2.[37,38] Despite highly granular in nature, film **1** showed good grains cohesion resulting in a continuous film. AFM images substantiated a non-directional growth and a RMS roughness around 4–4.5 nm (range of values resulted from the evaluation of various AFM images).

In order to improve the film quality, we tested an *in situ* Si(111) substrate thermal annealing (500 °C and 20 mbar under N_2 atmosphere for 1 h). Tilted cross-section SEM images of Sb_2Te_3 films deposited on the treated substrate ("Sb_2Te_3 – Substrate Annealing", **2**) clearly showed a film of enhanced crystallinity and significantly improved morphology; granularity was largely diminished to the extent that Sb_2Te_3 appeared as a continuous film no longer composed of juxtaposed grains of various sizes and, consequently, the surface roughness was lowered (RMS roughness of 1.5–1.8 nm) (Fig. 1).

Open Access Article. Published on 27 May 2020. Downloaded on 7/22/2020 1:37:40 PM. This article is licensed under a Creative Commons Attribution-NonCommercial 3.0 Unported Licence.

Open Access Article. Published on 27 May 2020. Downloaded on 7/22/2020 1:37:40 PM.
This article is licensed under a Creative Commons Attribution-NonCommercial 3.0 Unported Licence.

Fig. 1 (Left) Tilted cross-section SEM images, (center) AFM images (R_q values are specific to the shown AFM images), (Right) grains size distribution histograms (as determined by AFM) of Sb_2Te_3 – As Deposited (**1**) and Sb_2Te_3 – Substrate Annealing (**2**), and a selected AFM surface profile of Sb_2Te_3 – Post-Growth Annealing (**3**). See ESI (Fig. S1–S8†) for more SEM and AFM images.

AFM data highlighted interesting features in the fine structure of the films (Fig. 1). Sb_2Te_3 – As Deposited (**1**) exhibited a non-uniform granularity consisting of a bimodal grains size distribution centered at *ca.* 18 and 33 nm. On the other hand, the Sb_2Te_3 – Substrate Annealing (**2**) film could be described by a narrower distribution of smaller grains – mostly within the 11–14 nm range – specifically accountable for the lower surface roughness.

Aiming at further structural improvement, we performed an *in situ* post-growth treatment; the Sb_2Te_3 film **2** was subjected to a thermal annealing at 300 °C under N_2 atmosphere for 15 min, at a relatively high pressure (900 mbar) to prevent or minimize desorption phenomena (Fig. 1, "Sb_2Te_3 – Post-Growth Annealing", **3**). This post-growth processing step neither did alter the film thickness nor was detrimental to its uniformity. It triggered instead a reorganization of the grains throughout the film. Nevertheless, the most relevant feature happened to be the film orientation that, as qualitatively ascertained from SEM and AFM images, became highly uniform and well-defined, along with a further lowering of the roughness (RMS roughness of 0.9–1.3 nm). An AFM profile extracted from Sb_2Te_3 – Post-Growth Annealing (**3**) (Fig. 1) evidences steps of 1 nm (consistent with an antimony telluride quintuple layer), supporting an improved ordering with respect to the parent Sb_2Te_3 materials **1** and **2**.

The MOCVD average growth rate of 0.44 ± 0.01 nm min^{-1}, extrapolated from films prepared with different deposition times, resulted appreciably lower than literature values that fall within the 8–50 nm min^{-1} range.[33–35,45] However, dissimilar experimental conditions, including the choice of the precursors (their chemical reactivity), the higher deposition temperature (up to 450 °C), and the use of dihydrogen rather than an inert

Open Access Article. Published on 27 May 2020. Downloaded on 7/22/2020 1:37:40 PM. This article is licensed under a Creative Commons Attribution-NonCommercial 3.0 Unported Licence.

gas, can significantly impact the growth rate and are therefore accountable for the observed low values.

The morphology and structural properties of the films were studied in detail by performing TEM analyses. Typical cross-sectional high-resolution views of the three different types of samples are reported in Fig. 2, including the corresponding Fast Fourier Transform (FFT) (insets). In general, crystalline planes and van der Waals stacks were observed in all samples, although each one showed a different degree of ordering and orientations.

Amongst the three samples, Sb_2Te_3 – As Deposited (**1**) appeared to be the most granular and defective in nature (see also Fig. S9, ESI†). Its FFT also highlights the essentially random orientation of its grains, even though sometimes the *c*-axis was found to be almost perpendicular to the substrate. Consistently with the SEM and AFM data, the structure of Sb_2Te_3 – Substrate Annealing (**2**) revealed a much lower granularity and a more ordered growth. However, different crystallographic orientations were detected throughout the sample (Fig. S10, ESI†).

Lastly, Sb_2Te_3 – Post-Growth Annealing (**3**), in agreement with SEM and AFM results, appeared to be composed of larger building units (more details in Fig. S11, ESI†). The *c*-axis of the Sb_2Te_3 crystalline cell was almost always found to be perpendicular to the silicon substrate, while grains with very low misalignment were rarely observed. The van der Waals gaps of the Sb_2Te_3 quintuple layer structure are clearly visible and parallel to the substrate. The (003) periodicity along the *c*-axis, measured over many pictures, was 1 nm, consistently with the one calculated for the Sb_2Te_3 rhombohedral structure.

Regardless of the morphological and structural differences between the three films, their thickness, probed *via* XRR (see Fig. S23 and Table S1, ESI†), remained almost unchanged. In fact, films (**2**) and (**3**) showed thicknesses (32.5 and 32.0 nm, respectively) only slightly reduced respect to (**1**), fact that is principally explained by their higher crystallinity and enhanced packing.

Also, their composition, as determined from the ratio of the Sb and Te L_α lines detected by TXRF, was found consistent with the Sb_2Te_3 stoichiometry (Fig. S12 and S13, ESI†); similarly, XPS data of the various films (Fig. S14–S22, ESI†) are identical and consistent with literature values.[36]

XRD studies were undertaken to probe the Sb_2Te_3 films crystallinity and evaluate the relevance of the substrate annealing and post-growth processing on their structural

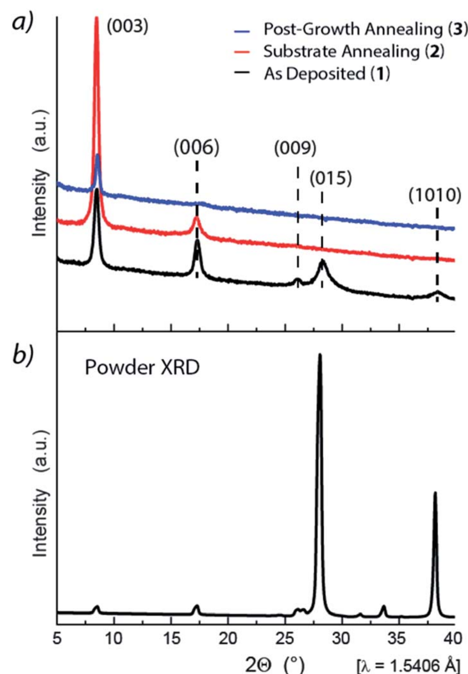

Fig. 3 (a) Grazing incidence X-ray diffraction pattern of (bottom, black) Sb_2Te_3 – As Deposited, (red, middle) Sb_2Te_3 – Substrate Annealing, and (blue, top) Sb_2Te_3 – Post-Growth Annealing; (b) powder XRD pattern reference for Sb_2Te_3 measured at RT and atmospheric pressure. Lattice parameters: $a = 4.264$ Å and $c = 30.458$ Å (*ICSD Inorganic Crystal Structure Database*, FIZ Karlsruhe, 2019, file no. 2084).[47]

properties. The Grazing Incidence X-ray Diffraction (GIXRD) pattern of **1** (Fig. 3a, black) exhibited intense reflections at $2\theta = 8.46°$, $17.3°$, $26.0°$, $28.26°$, and *ca.* $38.4°$ corresponding to the 003, 006, 009, 015, and 1 0 10 reflections, attributed to the rhombohedral crystalline structure in the $R\bar{3}m$ space group.

The relatively small linewidths of the (00ℓ) peaks indicated high crystallinity while the (015) peak – the peak with the highest intensity in the powder diffractogram[47] – indicated the polycrystalline nature of the film, and its broadening, possibly, a structural amorphous component.

Interestingly, the 015 reflection was no longer observed in the Sb_2Te_3 – Substrate Annealing (**2**) thin film (Fig. 3a, red), whereas the 003 reflection was drastically enhanced, indicative of grains predominantly oriented along the $[00\ell]$ direction and, consequently, of a more crystalline structure. Moreover, the

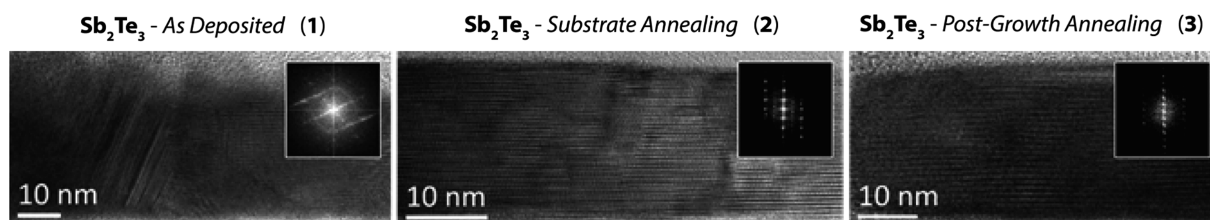

Fig. 2 Cross sectional high resolution TEM images of the Sb_2Te_3 films: Sb_2Te_3 – As Deposited (**1**), Sb_2Te_3 – Substrate Annealing (**2**), and Sb_2Te_3 – Post-Growth Annealing (**3**). Insets: fast Fourier transform analyses.

Open Access Article. Published on 27 May 2020. Downloaded on 7/22/2020 1:37:40 PM. This article is licensed under a Creative Commons Attribution-NonCommercial 3.0 Unported Licence.

GIXRD of the Sb_2Te_3 – Post-Growth Annealing (**3**) film revealed an overall reduction of the peaks intensity (Fig. 3a, blue) suggesting substantial changes in the structure, compatible with a crystallinity improvement.

To assess the Sb_2Te_3 crystalline nature, XRD measurements were set up specifically to probe out-of-plane and in-plane orientations.

The XRD patterns collected in the Bragg–Brentano geometry (Fig. 4a) revealed the scattering of the reflections' intensity across ω (plot's y-axis), feature informative of the broadening in the (00ℓ) out-of-plane orientation.

While the full width at half maximum (FWHM) of the ω scan, (see plots in Fig. 4a) was substantial in **1** (up to 9°), it appeared much reduced in **2** (2.6°) and strongly contained in **3** that showed an FWHM value of 0.46°, indicating a mosaicity typical of epitaxial films and suggestive of single crystal-like materials.

These data, along with the absence of the 015 reflection (both in **2** and **3**, consistently with the GIXRD – Fig. 3) indicated strongly (00ℓ) out-of-plane oriented grains in the Sb_2Te_3 – Post-Growth Annealing (**3**) film.

Moreover, the in-plane orientation, probed through a φ angle scan here optimized on the 015 reflection ($2\theta = 28.26°$), appeared positively affected by Substrate Annealing and Post-Growth Annealing, too (Fig. 4b). In fact, while **1** showed almost no in-plane ordering, 60°-spaced peaks distinctive of the 3-fold symmetry of the Sb_2Te_3 rhombohedral cell (and related to the 015 reflection) emerged in the 2θ–φ plot of **2**, as result of a preferential in-plane orientation (Fig. 4b). However, the faint line connecting the (015) peaks revealed residual disorder, indicative of a minor fraction of randomly oriented grains. Differently, the intense, precisely positioned, and narrow peaks of the 015 reflections observed in Sb_2Te_3 – Post-Growth Annealing (**3**) indicates an almost complete in-plane ordering (Fig. 4b). Combining the data from the Bragg–Brentano and the φ scan, the epitaxial relationship between the Sb_2Te_3 and the substrate is found as $Sb_2Te_3[00\ell]\|Si[111]$ and $Sb_2Te_3[015]\|Si[011]$. The latter epitaxial relationship was deduced by a careful positioning of the sample, in the way that the $\varphi = 0$ position corresponds to the Si[011] direction parallel to the X-ray beam (Fig. S24, ESI†).

The set of structural information attained from the microscopies and diffraction measurements can be rationalized as sketched in Fig. 4c. This visual representation highlights the structural and morphological transition from a highly granular and poorly oriented film (**1**) to a smoother and crystallographically out-of-plane ordered one (**2**), and, finally to an epitaxial layer, consisting of crystallites both in-plane and out-of-plane oriented (**3**).

The quality improvement observed comparing Sb_2Te_3 – As Deposited (**1**) and Sb_2Te_3 – Substrate Annealing (**2**) is the result

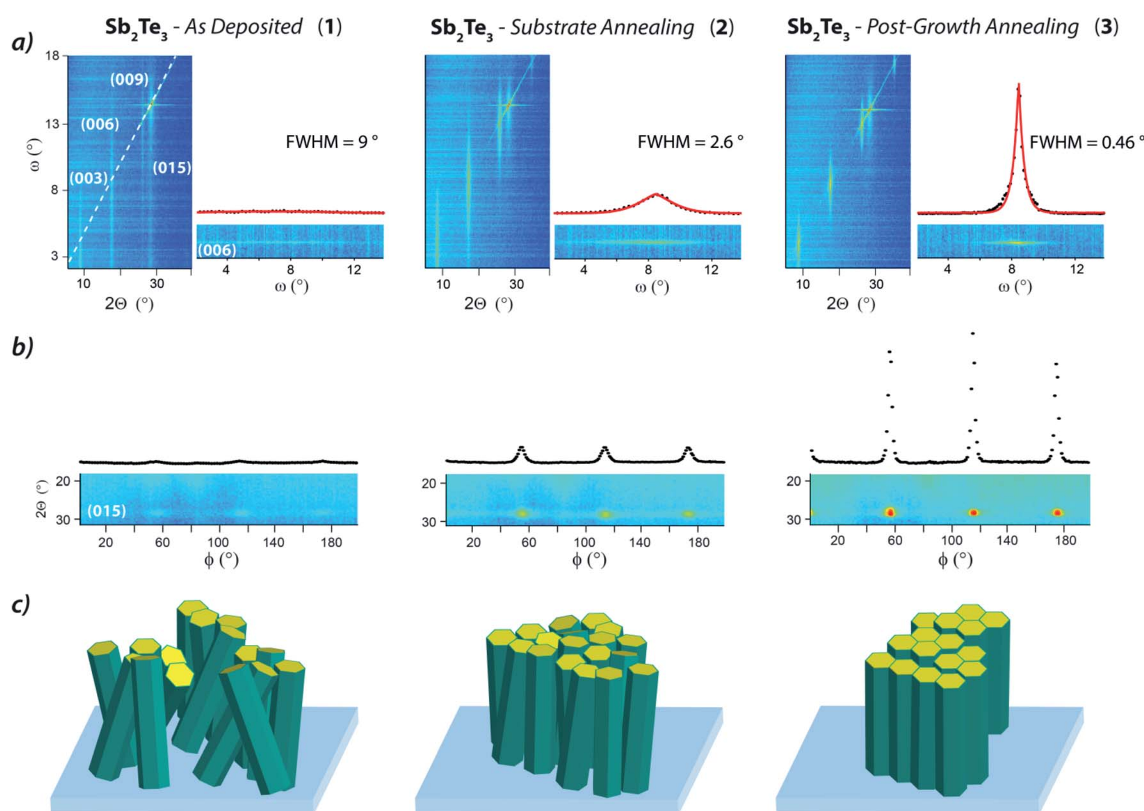

Fig. 4 (a) XRD pattern collected in Bragg–Brentano geometry, including the profile of the (006) peak and the mosaicity values, and (b) φ angle scan of Sb_2Te_3 – As Deposited (**1**), Sb_2Te_3 – Substrate Annealing (**2**), and Sb_2Te_3 – Post-Growth Annealing (**3**). The dashed line in (a) evidences the Bragg–Brentano condition. The most intense signal in (a) is the 111 reflection pertaining to the silicon substrates and it is very close to the (015) peak. (c) Graphical representation of the Sb_2Te_3 crystalline ordering and orientation relative to the Si(111) substrate.

 This journal is © The Royal Society of Chemistry 2020

Open Access Article. Published on 27 May 2020. Downloaded on 7/22/2020 1:37:40 PM. This article is licensed under a Creative Commons Attribution-NonCommercial 3.0 Unported Licence.

of the Si(111) substrate annealing. A high temperature substrate treatment likely favors the removal of adventitious physisorbed or chemisorbed water, preventing from a disorderly initial-stage deposition, whereas we tend to exclude surface reconstruction phenomena that are known to take place at higher temperatures.[48,49]

In fact, as the MOCVD process was performed at room temperature, therefore not requiring the precursors' pyrolysis, residual surface water and hydroxyl groups would readily react with the protolyzable organometallic precursors, compromising the integrity of the silicon/Sb_2Te_3 interfacial van der Waals layers and possibly resulting in an uncontrolled deposition and an unordered and highly granular growth.

While some structural enhancement (out-of-plane orientation) was obtained upon substrate annealing, the most remarkable improvement was indeed achieved with the post-growth processing. This step is specifically responsible for the in-plane ordering. We speculate that the thermal treatment triggers a rearrangement of the grains into a thermodynamically preferred configuration allowed by the symmetry match between the substrate and the film. The crystallites preferential orientation is possibly induced by the surface-exposed crystalline lattice of Si(111). The working hypothesis for the selection of Si(111) as preferred substrate in the present study relies indeed on its surface lattice symmetry, analogous to the Sb_2Te_3 crystalline cell.

Conclusion

We grew antimony telluride continuous thin films by an MOCVD process unusually conducted at room temperature and described a successful approach to gain control over the structural quality of the films.

Substrate annealing and post-growth annealing are found to effectively control the granularity, lower the roughness, and allow the growth of Sb_2Te_3 films on a highly lattice-mismatched substrate; nevertheless, the resulting thin films are highly oriented along the $[00\ell]$ direction, concomitantly with a specific in-plane crystalline order, a feature typical of an epitaxial growth.

This process appears therefore suitable for large scale preparation of epitaxial Sb_2Te_3 on Si(111), a substrate commonly adopted in microelectronics and for devices implementation.

Conflicts of interest

There are no conflicts to declare.

Acknowledgements

We acknowledge the Horizon 2020 project SKYTOP "Skyrmion-Topological Insulator and Weyl Semimetal Technology" (FETPROACT-2018-01, no. 824123).

Notes and references

1 S. Manzeli, D. Ovchinnikov, D. Pasquier, O. V. Yazyev and A. Kis, *Nat. Rev. Mater.*, 2017, **2**, 17033.
2 M. Longo, O. Salicio, C. Wiemer, R. Fallica, A. Molle, M. Fanciulli, C. Giesen, B. Seitzinger, P. K. Baumann, M. Heuken and S. Rushworth, *J. Cryst. Growth*, 2008, **310**, 5053–5057.
3 T. P. Ginley, Y. Wang and S. Law, *Crystals*, 2016, **6**, 154.
4 P. Guo, A. M. Sarangan and I. Agha, *Appl. Sci.*, 2019, **9**, 530.
5 M. Longo, T. Stoycheva, R. Fallica, C. Wiemer, L. Lazzarini and E. Rotunno, *J. Cryst. Growth*, 2013, **370**, 323–327.
6 E. Rotunno, M. Longo, C. Wiemer, R. Fallica, D. Campi, M. Bernasconi, A. R. Lupini, S. J. Pennycook and L. Lazzarini, *Chem. Mater.*, 2015, **27**, 4368–4373.
7 S. Selmo, S. Cecchi, R. Cecchini, C. Wiemer, M. Fanciulli, E. Rotunno, L. Lazzarini and M. Longo, *Phys. Status Solidi A*, 2016, **213**, 335–338.
8 N. Zibouche, A. Kuc, J. Musfeldt and T. Heine, *Ann. Phys.*, 2014, **526**, 395–401.
9 J. E. Boschker and R. Calarco, *Adv. Phys.: X*, 2017, **2**, 675–694.
10 D. Campi, L. Paulatto, G. Fugallo, F. Mauri and M. Bernasconi, *Phys. Rev. B*, 2017, **95**, 024311.
11 R. Venkatasubramanian, E. Siivola, T. Colpitts and B. O'Quinn, *Nature*, 2001, **413**, 597–602.
12 S. Zastrow, J. Gooth, T. Boehnert, S. Heiderich, W. Toellner, S. Heimann, S. Schulz and K. Nielsch, *Semicond. Sci. Technol.*, 2013, **28**, 035010.
13 Y. V. Ivanov, A. T. Burkov and D. A. Pshenay-Severin, *Phys. Status Solidi B*, 2018, **255**, 1800020.
14 H. Zhang, C.-X. Liu, X.-L. Qi, X. Dai, Z. Fang and S.-C. Zhang, *Nat. Phys.*, 2009, **5**, 438–442.
15 J. J. Cha, K. J. Koski and Y. Cui, *Phys. Status Solidi RRL*, 2013, **7**, 15–25.
16 G.-H. Dong, Y.-J. Zhu and L.-D. Chen, *CrystEngComm*, 2011, **13**, 6811–6816.
17 Y. Saito, P. Fons, A. V. Kolobov and J. Tominaga, *Phys. Status Solidi B*, 2015, **252**, 2151–2158.
18 Y. Saito, P. Fons, L. Bolotov, N. Miyata, A. V. Kolobov and J. Tominaga, *AIP Adv.*, 2016, **6**, 045220.
19 P. Marchand, I. A. Hassan, I. P. Parkin and C. J. Carmalt, *Dalton Trans.*, 2013, **42**, 9406–9422.
20 S. L. Benjamin, C. H. de Groot, A. L. Hector, R. Huang, E. Koukharenko, W. Levason and G. Reid, *J. Mater. Chem. C*, 2015, **3**, 423–430.
21 V. Pore, T. Hatanpää, M. Ritala and M. Leskelä, *J. Am. Chem. Soc.*, 2009, **131**, 3478–3480.
22 K. Knapas, T. Hatanpää, M. Ritala and M. Leskelä, *Chem. Mater.*, 2010, **22**, 1386–1391.
23 D. Nminibapiel, K. Zhang, M. Tangirala, H. Baumgart, V. S. K. Chakravadhanula, C. Kübel and V. Kochergin, *ECS J. Solid State Sci. Technol.*, 2014, **3**, P95–P100.
24 V. Pore, K. Knapas, T. Hatanpää, T. Sarnet, M. Kemell, M. Ritala, M. Leskelä and K. Mizohata, *Chem. Mater.*, 2011, **23**, 247–254.

Open Access Article. Published on 27 May 2020. Downloaded on 7/22/2020 1:37:40 PM.
This article is licensed under a Creative Commons Attribution-NonCommercial 3.0 Unported Licence.

25 T. Eom, T. Gwon, S. Yoo, B. J. Choi, M.-S. Kim, S. Ivanov, A. Adamczyk, I. Buchanan, M. Xiao and C. S. Hwang, *J. Mater. Chem. C*, 2015, **3**, 1365–1370.

26 L. Zheng, X. Cheng, D. Cao, Q. Wang, Z. Wang, C. Xia, L. Shen, Y. Yu and D. Shen, *RSC Adv.*, 2015, **5**, 40007–40011.

27 G. Wang, X. Zhu, J. Wen, X. Chen, K. He, L. Wang, X. Ma, Y. Liu, X. Dai, Z. Fang, J. Jia and Q. Xue, *Nano Res.*, 2010, **3**, 874–880.

28 N. Peranio, M. Winkler, D. Bessas, Z. Aabdin, J. König, H. Böttner, R. P. Hermann and O. Eibl, *J. Alloys Compd.*, 2012, **521**, 163–173.

29 J. Kampmeier, C. Weyrich, M. Lanius, M. Schall, E. Neumann, G. Mussler, T. Schäpers and D. Grützmacher, *J. Cryst. Growth*, 2016, **443**, 38–42.

30 F. Bonell, M. G. Cuxart, K. Song, R. Robles, P. Ordejón, S. Roche, A. Mugarza and S. O. Valenzuela, *Cryst. Growth Des.*, 2017, **17**, 4655–4660.

31 R. Venkatasubramanian, T. Colpitts, B. O'Quinn, S. Liu, N. El-Masry and M. Lamvik, *Appl. Phys. Lett.*, 1999, **75**, 1104–1106.

32 A. Giani, A. Boulouz, F. Pascal-Delannoy, A. Foucaran, E. Charles and A. Boyer, *Mater. Sci. Eng., B*, 1999, **64**, 19–24.

33 G. Bendt, S. Schulz, S. Zastrow and K. Nielsch, *Chem. Vap. Deposition*, 2013, **19**, 235–241.

34 G. Bendt, S. Zastrow, K. Nielsch, P. S. Mandal, J. Sánchez-Barriga, O. Rader and S. Schulz, *J. Mater. Chem. A*, 2014, **2**, 8215–8222.

35 P. I. Kuznetsov, B. S. Shchamkhalova, V. O. Yapaskurt, V. D. Shcherbakov, V. A. Luzanov, G. G. Yakushcheva, V. A. Jitov and V. E. Sizov, *J. Cryst. Growth*, 2017, **471**, 1–7.

36 A. A. Volykhov, J. Sánchez-Barriga, A. P. Sirotina, V. S. Neudachina, A. S. Frolov, E. A. Gerber, E. Y. Kataev, B. Senkovsky, N. O. Khmelevsky, A. Y. Aksenenko, N. V. Korobova, A. Knop-Gericke, O. Rader and L. V. Yashina, *Chem. Mater.*, 2016, **28**, 8916–8923.

37 R. Cecchini, R. Mantovan, C. Wiemer, L. Nasi, L. Lazzarini and M. Longo, *Phys. Status Solidi RRL*, 2018, **12**, 1800155.

38 E. Longo, C. Wiemer, R. Cecchini, M. Longo, A. Lamperti, A. Khanas, A. Zenkevich, M. Fanciulli and R. Mantovan, *J. Magn. Magn. Mater.*, 2019, **474**, 632–636.

39 E. Longo, R. Mantovan, R. Cecchini, M. D. Overbeek, M. Longo, G. Trevisi, L. Lazzarini, G. Tallarida, M. Fanciulli, C. H. Winter and C. Wiemer, *Nano Res.*, 2020, **13**, 570–575.

40 R. D. Dupuis, *J. Cryst. Growth*, 1997, **178**, 56–73.

41 T. Detchprohm, J.-H. Ryou, X. Li and R. D. Dupuis, in *Metalorganic Vapor Phase Epitaxy (MOVPE)*, ed. S. Irvine and P. Capper, Wiley, Haboken, NJ, 2020, ch. 14, pp. 507–548.

42 G. Bendt, K. Kaiser, A. Heckel, F. Rieger, D. Oing, A. Lorke, N. P. Rodriguez, G. Schierning, C. Jooss and S. Schulz, *Semicond. Sci. Technol.*, 2018, **33**, 105002.

43 F. Rieger, V. Roddatis, K. Kaiser, G. Bendt, S. Schulz and C. Jooss, *Phys. Rev. Mater.*, 2020, **4**, 025402.

44 G. Bendt, J. Sonntag, A. Lorke, W. Assenmacher, U. Hagemann and S. Schulz, *Semicond. Sci. Technol.*, 2015, **30**, 085021.

45 T. J. Groshens, R. W. Gedridge Jr and C. K. Lowe-Ma, *Chem. Mater.*, 1994, **6**, 727–729.

46 T. J. Groshens, R. W. Gedridge, R. Scheri and T. Cole, in *Fifteenth International Conference on Thermoelectrics. Proceedings ICT '96*, 1996, pp. 430–434.

47 FIZ Karlsruhe, ICSD Inorganic Crystal Structure Database, 2019, file no. 2084.

48 R. J. Phaneuf, E. D. Williams and N. C. Bartelt, *Phys. Rev. B: Condens. Matter Mater. Phys.*, 1988, **38**, 1984–1993.

49 Y.-L. Wang, H.-M. Guo, Z.-H. Qin, H.-F. Ma and H.-J. Gao, *J. Nanomater.*, 2008, **2008**, 874213.

This journal is © The Royal Society of Chemistry 2020